Spontaneous Valley Spirals in Magnetically Encapsulated Twisted Bilayer Graphene

Tobias M. R. Wolf,[1,*] Oded Zilberberg,[1] Gianni Blatter,[1] and Jose L. Lado[2]
[1]Institute for Theoretical Physics, ETH Zurich, 8093 Zurich, Switzerland
[2]Department of Applied Physics, Aalto University, 00076 Aalto, Espoo, Finland

(Received 21 August 2020; accepted 7 January 2021; published 4 February 2021)

Van der Waals heterostructures provide a rich platform for emergent physics due to their tunable hybridization of layers, orbitals, and spin. Here, we find that twisted bilayer graphene stacked between antialigned ferromagnetic insulators can feature flat electronic bands due to the interplay between twist, exchange proximity, and spin–orbit coupling. These flat bands are nearly degenerate in valley only and are effectively described by a triangular superlattice model. At half filling, we find that interactions induce spontaneous valley correlations that favor spiral order and derive a low-energy valley-Heisenberg model with symmetric and antisymmetric exchange couplings. We also show how electric interlayer bias broadens the bands and tunes these couplings. Our results put forward magnetic van der Waals heterostructures as a platform to explore valley-correlated states.

DOI: 10.1103/PhysRevLett.126.056803

Twisted graphene multilayers have risen as a versatile platform for engineering correlated states of matter. Their unique flexibility stems from a new tunable length scale, the moiré length, which generates electronic minibands with a controllable ratio between kinetic and interaction energies. As a result, a variety of strongly correlated states appear in these twisted van der Waals materials, such as intrinsic superconductivity [1–4], strange metal behavior [5], and correlated insulators [6]. Furthermore, this platform can realize correlated states that are rarely found in nature, such as ferromagnetic superconductivity [7] and interaction-driven quantum anomalous Hall effect [8].

Thus far, investigations into correlated states of twisted graphene multilayers mostly focus on spontaneous symmetry-breaking of the spin ($\pm 1/2$) degree of freedom, i.e., of the symmetry group $\mathrm{SU}(2)_s$ [9]. Interestingly, low-energy charge carriers in graphene also have two valleys (K, K') as orbital quantum number with $\mathrm{U}(1)_v$ symmetry [or approximately $\mathrm{SU}(2)_v$ [10–13]]. This offers additional possibilities for symmetry breaking due to interactions, e.g., spontaneous valley-polarized [8] or valley-coherent [14,15] states, which can become relevant in the context of superconductivity [16,17]. Here, we show that proximity-induced spin–orbit coupling can lock spin and valley in a way that promotes spontaneous symmetry breaking in the valley sector with spatial valley textures.

Spin–orbit coupling (SOC) in graphene engenders topological phenomena such as the quantum spin Hall effect [18] and the quantum anomalous Hall effect [19,20]. The negligible intrinsic SOC in graphene [21] can be strongly enhanced extrinsically [22–27], e.g., through proximity to other van der Waals materials. For example, transition metal dichalcogenides (TMDs) have been shown to induce Rashba SOC as large as 15 meV and spin–valley SOC of the order of 1.5 meV on a neighboring graphene layer [26]. Ferromagnetic insulators, such as CrI_3, have been predicted to induce similar SOC enhancement, in addition to sizable magnetic exchange fields [19,28]. In twisted graphene bilayers, the energy scale of the spin–orbit coupling should be compared with a typical correlation gap that lies between 0.3 [6] and 8 meV [29]. Even though the Rashba SOC can compete with these correlated gaps, this interplay has thus far not received much attention in twisted van der Waals materials.

In this Letter, we focus on the valley degree of freedom, described as a two spinor and demonstrate correlations in the valley spinor of twisted bilayer graphene encapsulated within ferromagnetic insulators (FIs) with layer-antiferromagnetic alignment, see Fig. 1(a). We show that the combination of twist alongside proximity-induced magnetic exchange and Rashba spin–orbit coupling hybridizes the spins and leads to valley-degenerate flatbands. It is this valley degeneracy without spin degeneracy that provides a unique playground for symmetry-broken states solely in the valley sector. For the latter, we propose a phenomenological lattice model that captures the low-energy flatband valley physics. At half filling of the flatbands, we find that screened interactions favor valley-spiral order and derive an anisotropic valley-Heisenberg model with exchange couplings that are controllable through electric interlayer bias. We discuss potential experimental scenarios to detect this effect. Notably, the mechanism by which we induce nearly valley-degenerate flatbands through magnetic proximity readily extends to other twisted graphene multilayers with flatbands.

We consider twisted bilayer graphene encapsulated between ferromagnetic insulators, see Fig. 1(a). We describe the electronic properties of the system using an

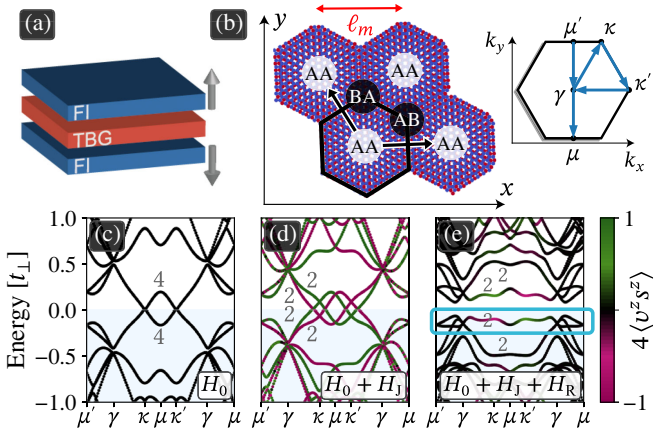

FIG. 1. Structure and single-particle electronic properties of twisted bilayer graphene (TBG) encapsulated between ferromagnetic insulators, see (a) where arrows denote the magnetization of each FI. (b) Moiré pattern arising from stacking two graphene layers with relative twist angle α. The pattern has a length scale ℓ_m with AA, AB, and BA regions. It generates a hexagonal mini-Brillouin zone with high-symmetry points. (c)–(e) Band structures at twist angle $\alpha \simeq 2°$, interlayer coupling $t_\perp = 0.12t$, and no interlayer bias ($V = 0$): for (c) the isolated TBG, including (d) local exchange fields with $m = t_\perp/3$, and including (e) both exchange fields with $m = t_\perp/3$ and Rashba SOC $\lambda_R = t_\perp/3$. The band colors indicate the expectation value of the valley-spin operator $\langle v^z s^z \rangle$, showing fixed spin and valley in (d) and finite spin mixing at fixed valley in (e). The light blue box marks the flatband below charge neutrality.

atomistic tight-binding Hamiltonian for the graphene bilayer,

$$H = H_0 + H_J + H_R, \tag{1}$$

to which the FI effectively contributes through virtual tunneling [20,30–35]. The Hamiltonian H_0 describes the bare twisted bilayer, H_J includes proximity-induced exchange fields, and H_R contains proximity-induced Rashba spin–orbit couplings [36–38], which strongly break inversion symmetry in each graphene layer. The bare bilayer Hamiltonian is $H_0 = \sum_{\langle i,j\rangle,s} t c^\dagger_{i,s} c_{j,s} + \sum_{i,j,s} t^\perp_{ij} c^\dagger_{i,s} c_{j,s} - \sum_{i,s} V_i c^\dagger_{i,s} c_{i,s}$, where $c^{(\dagger)}_{i,s}$ destroys (creates) an electron with spin $s \in \{\pm 1/2\}$ at position $\boldsymbol{r}_i = (x_i, y_i, z_i)$ in one of the layers located at $z_i = \pm d/2$. We consider nearest-neighbor hopping with amplitude $t \simeq -2.7$ eV [39]. The interlayer hopping from site $\boldsymbol{r}_i$ to $\boldsymbol{r}_j$ is parametrized as $t^\perp_{ij} = t_\perp[(z_i - z_j)^2/|\boldsymbol{r}_i - \boldsymbol{r}_j|^2] e^{-(|\boldsymbol{r}_i - \boldsymbol{r}_j| - d)/\ell}$, with $t_\perp \simeq 0.12t$ that describes the hybridization over the interlayer distance $d \simeq 2.35a_0$, with a_0 the intralayer bond length and $\ell \simeq 0.3a_0$ controlling the hopping range [40–42]. The potentials $V_i = \mu + \mathrm{sgn}(z_i)V$ describe the overall chemical potential μ and electric interlayer bias V.

We first discuss the system in the absence of interlayer bias, $V = 0$. Each isolated graphene layer $l \in \{1, 2\}$ features Dirac-like band touchings at valleys K, K' [39], which we label with the eigenvalues $v \in \{\pm 1/2\}$ of the valley operator v^z [43–46]. The decoupled bilayer has eightfold degenerate bands characterized by valley v, spin s, and layer l; the latter gets hybridized by interlayer coupling. A finite twist angle α between the layers leads to a moiré structure with a characteristic length ℓ_m and regions labeled AA and AB/BA in accord with the vertical alignment of the A and B sites between layers, see Fig. 1(b). The resulting superlattice implies that the spectrum of H_0 consists of many minibands, resulting from backfolding the dispersion of each graphene layer and subsequent interlayer hybridization [47], see Fig. 1(c). For a large moiré length ℓ_m and low energies, intervalley scattering is negligible such that each miniband at Bloch momentum $\boldsymbol{k}$ (in valley K) is spin degenerate and has a valley partner at $-\boldsymbol{k}$ (in valley K'). Hence, each eigenvalue is fourfold degenerate [48–52] or higher along high-symmetry lines in the mini-Brillouin zone (BZ). These low-energy minibands are typically dispersive, except for fine-tuned angles [46,49,51,53–56] or in the limit of tiny twist angles [44,52].

The encapsulation of TBG between ferromagnetic insulators with layer-antiferromagnetic alignment [cf. Fig. 1(a)] profoundly alters the low-energy spectrum. The FIs induce exchange fields with moments $\boldsymbol{m}_i = \mathrm{sgn}(z_i) m \hat{\boldsymbol{z}}$ at each site $\boldsymbol{r}_i$ and generate Rashba spin–orbit couplings $\lambda_{R,i} = \mathrm{sgn}(z_i)\lambda_R$ in each graphene layer [57], see Supplemental Material [58] for a discussion of other SOCs. They are described by $H_J = \sum_{j,ss'} (\boldsymbol{m}_j \cdot \boldsymbol{\sigma})_{ss'} c^\dagger_{j,s} c_{j,s'}$, and $H_R = i \sum_{\langle i,j\rangle,ss'} \lambda_{R,i} \times (\boldsymbol{\sigma} \times \boldsymbol{d}_{ij})^z_{ss'} c^\dagger_{i,s} c_{j,s'}$, respectively, where $\boldsymbol{d}_{ij}$ is the bond vector connecting intralayer sites i, j and the components of $\boldsymbol{\sigma} = (\sigma^x, \sigma^y, \sigma^z)$ are Pauli matrices for spin. Given the layer-antiferromagnetic alignment of our FIs, the exchange fields $\boldsymbol{m}_i$ act as a (spin-dependent) magnetic interlayer bias [59]. Interestingly, while the exchange field breaks time-reversal symmetry, the eigenstates are degenerate between spin-$\uparrow$ bands of one valley (say K) and spin-$\downarrow$ of the other (say K'), see Fig. 1(d), which follows from symmetry under a layer-exchanging, twofold rotation and time reversal. The Rashba coupling λ_R, however, mixes the two spin channels, introduces a sizable hybridization gap around charge neutrality and flattens the otherwise dispersive bands, see Fig. 1(e).

As a result, the FI-encapsulated twisted bilayer features a van Hove singularity adjacent to the energy gap at charge neutrality. This singularity is most pronounced for a fine-tuned ratio $\alpha/t_\perp$ between twist angle and the interlayer coupling, here corresponding to physical parameters $\alpha \approx 2°$, $t_\perp = 0.12t$, when $m = t_\perp/3$, $\lambda_R = t_\perp/3$ [58]. The corresponding bands then become maximally flat, see Fig. 1(e), and their wave functions are concentrated within the AA region of the moiré unit cell, see Fig. 2(a). Importantly, these bands are only degenerate in the *valley* degree of freedom, whereas spin is fully hybridized—in contrast to other graphene multilayer systems, where spin degeneracies persist [50].

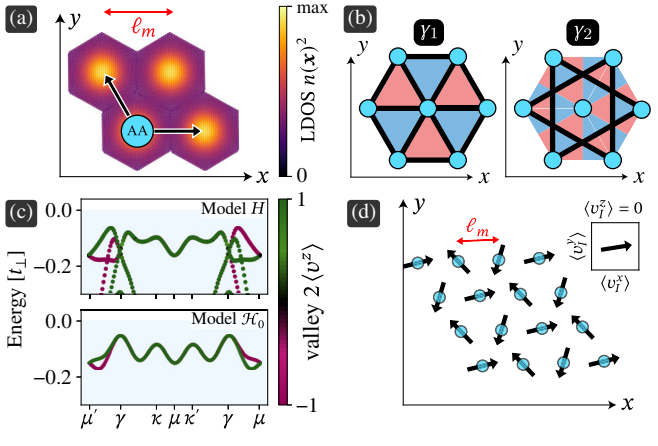

FIG. 2. Effective triangular lattice model for the moiré orbitals of the flatband. (a) Integrated local density of states $n(E,\boldsymbol{x})$ squared of the flatband marked in Fig. 1(e), with AA regions highlighted. (b) A sketch of the lattice model $\mathcal{H}_0$, see Eq. (2), where cyan circles represent the AA regions, the black lines denote hoppings γ_1, γ_2, respectively, and the red and blue triangles represent the staggered flux patterns associated with corresponding hopping phases ϕ_1 and ϕ_2. (c, top) Closeup on the flatband in Figs. 1(e) and 1(c, bottom) comparison with the band of the phenomenological model [cf. Eq. (2) with $\gamma_1/t_\perp = 0.03$, $\gamma_2/t_\perp = 0.09$, $\phi_1 = 0$, $\phi_2 = -0.4$]. The band color indicates the valley index $v = \langle v^z\rangle$ and illustrates the valley degeneracy along γ-κ-κ'-γ (green on top of magenta). (d) (In-plane) valley spiral appearing in the mean-field ground state of $\mathcal{H}_0 + \mathcal{H}_U$, cf. Eqs. (2) and (3). Arrows illustrate the valley polarization $\langle \boldsymbol{\nu}_I\rangle$ of the respective moiré Wannier orbital (inset).

These flatbands can be derived from a simple effective model describing hopping between Wannier moiré orbitals arranged in a triangular superlattice, see Fig. 2(b), i.e.,

$$\mathcal{H}_0 = \sum_{\langle IJ\rangle} \gamma_1 \psi_I^\dagger e^{i\tau^z \nu_{IJ}\phi_1} \psi_J + \sum_{\langle\langle IJ\rangle\rangle} \gamma_2 \psi_I^\dagger e^{i\tau^z \nu_{IJ}\phi_2} \psi_J, \quad (2)$$

with Pauli matrices $\tau^{x,y,z}$ for valley, valley spinors $\psi_I^{(\dagger)} = (d_{I,1/2}^{(\dagger)}, d_{I,-1/2}^{(\dagger)})$, and destruction (creation) operators $d_{I,v}^{(\dagger)}$ for electrons in moiré unit cells I, with valley index $v \in \{\pm 1/2\}$ taking the role of a pseudospin. The form of the hopping amplitudes follows from symmetry arguments [58], and we include first- and second-neighbor amplitudes $\gamma_{1,2} > 0$ with phases $\phi_{1,2}$ and signs $\nu_{IJ} = -\nu_{JI} \in \{\pm 1\}$ that ensure symmetry under rotation by $2\pi/3$, see Fig. 2(b). Similar complex-valued hopping amplitudes appear in the Kane-Mele model [18] due to spin–orbit coupling, such that we refer to $\phi_{1,2}$ as "valley–orbit phases" in our model by analogy. In the absence of interlayer bias, symmetry enforces real first-neighbor hopping ($\phi_1 = 0$) [58], whereas ϕ_2 is finite in general. The hopping parameters can then be chosen to qualitatively reproduce the flatband, see Fig. 2(c). We will see how interlayer bias affects this low-energy model later.

The presence of flatbands naturally raises the question of how interactions affect the corresponding electronic states near half filling. In our bilayer, this corresponds to doping with one electron or hole per moiré unit cell. When the screened Coulomb interactions between the atoms in the twisted bilayer are shorter ranged than the moiré length ℓ_m [58,60–63], the effective interaction between the moiré orbitals in (2) becomes

$$\mathcal{H}_U = \frac{U}{2} \sum_{I,v} n_{I,v} n_{I,-v}, \quad (3)$$

where $n_{I,v} = d_{I,v}^\dagger d_{I,v}$ is the number operator for valley v of moiré orbital I and $U \simeq 0.15 t_\perp$ [60] is the Hubbard interaction strength. Our effective model $\mathcal{H} = \mathcal{H}_0 + \mathcal{H}_U$ differs from the conventional Fermi-Hubbard model [64] in two respects: First, we have valley as pseudospin and, second, our hopping amplitudes are complex. In what follows, we consider half filling, such that the expected occupation number is $\langle n_I\rangle = 1$, and calculate the valley order of the ground state, which we characterize by the expectation value of the valley operator $\boldsymbol{\nu}_I = \psi_I^\dagger \boldsymbol{\tau} \psi_I/2$ in each moiré cell I. We can interpret $\langle v_I^z\rangle$ as the local valley imbalance and $\langle v_I^{x,y}\rangle$ as local valley coherence. We will see that, similar to other spin-1/2 triangular lattice models [65–68], our model $\mathcal{H}$, cf. Eqs. (2) and (3), is prone to valley-spiral states [see Fig. 2(d)] and that valley–orbit coupling can promote anisotropic exchange [66].

We determine the ground state using a self-consistent mean-field approximation, i.e., $\mathcal{H}_U \approx \sum_I \psi_I^\dagger \bar{U}(\rho^I)\psi_I - E_0(\rho^I)$, with the density matrix $\rho^I = \langle n_I\rangle/2 + \langle \boldsymbol{\nu}_I\rangle \cdot \boldsymbol{\tau}$ and the mean-field interaction $\bar{U}(\rho^I)$ and shift $E_0(\rho^I)$ [58]. Performing self-consistent relaxation of different initial states, we find that interactions and geometrical frustration in the triangular lattice favor a valley-spiral state on the length scale of the moiré structure, see Fig. 2(d). We find that (i) the length scale of the spiral varies slightly with the ratio γ_2/γ_1, and (ii) the spiral favors planar configurations with $\langle v_I^z\rangle = 0$. Hence, the valleys seek a state with equal occupation $\langle n_{I,K}\rangle = \langle n_{I,K'}\rangle$ and mix coherently, $\langle v_I^{x,y}\rangle \neq 0$. Interestingly, in the limit $\phi_2 \to 0$, stabilization of the in-plane spiral state is lost such that states with finite components $\langle v_I^z\rangle > 0$ become degenerate with in-plane configurations; this suggests that the phases ϕ_1 and ϕ_2 in $\mathcal{H}_0$ [see Eq. (2) and Fig. 2(b)] play a crucial role in defining the valley order.

To better understand our mean-field results, we expand the Hamiltonian $\mathcal{H}$ at half filling in the strong-interaction limit $U \gg \gamma_1, \gamma_2$ using a Schrieffer-Wolff transformation [58,69], resulting in a valley-Heisenberg model with anisotropic and (anti)symmetric exchange, i.e.,

$$\mathcal{H}_v = \sum_{IJ} J_{IJ} \boldsymbol{\nu}_I \cdot \boldsymbol{\nu}_J + \Delta_{IJ} v_I^z v_J^z + \nu_{IJ} D_{IJ} (\boldsymbol{\nu}_I \times \boldsymbol{\nu}_J)_z. \quad (4)$$

Here, J_{IJ}, Δ_{IJ}, and D_{IJ} denote the isotropic, anisotropic, and antisymmetric exchange couplings, respectively. These couplings are finite for first- and second-neighbor exchange only (indexed by $n = 1, 2$) and take the form $J_n = J_n^0(\cos^2\phi_n - \sin^2\phi_n)$, $\Delta_n = 2J_n^0\sin^2\phi_n$, and $D_n = J_n^0\sin(2\phi_n)$, with $J_n^0 = 2\gamma_n^2/U$. In the absence of an interlayer bias ($V = 0$), we have $\phi_1 = 0$ such that the first-neighbor terms in $\mathcal{H}_v$ are isotropic. Generally, the isotropic exchange couplings J_n can turn valley magnetic [70] ($J_n < 0$) as ϕ_n increases; however, for the regimes we consider here, we restrict ourselves to anti-valley-magnetic couplings ($J_n > 0$ for $n = 1, 2$), which favors valley spirals due to geometric frustration in the triangular lattice. The finite phase ϕ_2 in the second-neighbor coupling stabilizes in-plane valley configurations by inducing anisotropy $\Delta_2 > 0$ and favors second-neighbor valley misalignment (canting) due to the antisymmetric coupling $D_2 > 0$. Note that the alternating nature of the signs $\nu_{IJ} \in \{\pm 1\}$ in our triangular lattice favors valley spirals as well, rather than chiral structures such as skyrmions [71]. Consequently, there are two distinct mechanisms driving valley spirals, such that the length scale of the valley spiral depends on the competition between anti-valley-magnetic geometric frustration (J_n, $n = 1, 2$) and the antisymmetric couplings (D_n, $n = 1, 2$). In the following, we investigate how the addition of a finite electric interlayer bias modifies the results discussed thus far.

Including a finite interlayer bias $V > 0$ in Eq. (1) induces effective valley-dependent fluxes $v\Phi(\boldsymbol{r}_i, E)$ in real space that remove the valley degeneracy, see Fig. 3(b); within the low-energy model $\mathcal{H}_0$ (2), they modify the valley–orbit phases ϕ_1 and ϕ_2. This is formalized by defining the valley flux of low-energy states [46,72,73] near the energy E and at position $\boldsymbol{r}_i$ as

$$\Phi(\boldsymbol{r}_i, E) = \int_{\mathrm{BZ}} \frac{d^2\boldsymbol{k}}{(2\pi)^2}\frac{\epsilon_{\alpha\beta}}{2}\langle \boldsymbol{r}_i|G(\partial_{k_\alpha}G^{-1})(\partial_{k_\beta}G)|\boldsymbol{r}_i\rangle, \qquad (5)$$

where $G = [E - H(\boldsymbol{k}) + i0^+]^{-1}\mathcal{P}$ is the valley Green's function with valley-polarization operator $\mathcal{P} = 2v^z$, and $\epsilon_{\alpha\beta}$ denotes the Levi-Civita symbol. For our flatbands, we find that the interlayer bias induces a staggered valley flux, see Fig. 3(a). This flux enters the low-energy model $\mathcal{H}_0$ (2), through a Peierls substitution, i.e., $\gamma_n \mapsto \gamma_n(V)e^{i\tau^z\phi_n(V)}$ for $n = 1, 2$, cf. Fig. 2(b). It contributes dominantly to ϕ_1 and provides a correction to ϕ_2 accounting for the tilt in the pattern. The bands of the effective model $\mathcal{H}_0(V)$ obtained in this way agree with the bands of the tight-binding Hamiltonian (1), see Fig. 3(b).

Consequently, the interlayer bias controls the effective valley-exchange couplings in model $\mathcal{H}_v$ (4) through the induced valley–orbit couplings $\phi_1(V)$ and $\phi_2(V)$. In Figs. 3(c)–3(e), we see that the couplings J_1, Δ_2, and D_2 do not change significantly with increasing bias V, while the coupling J_2 decreases substantially and Δ_1 and D_1 both turn

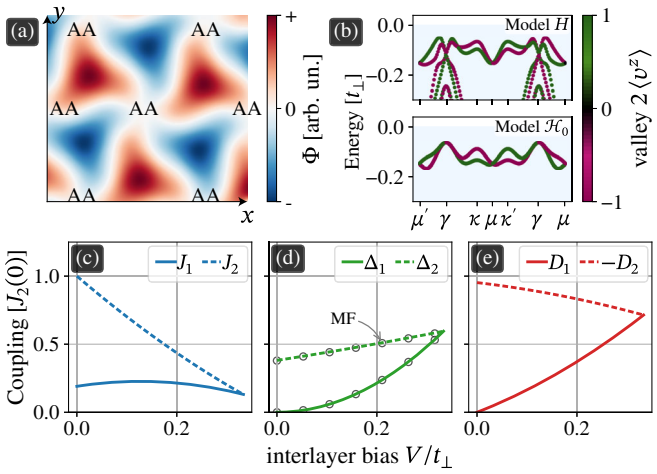

FIG. 3. Effect of interlayer bias V on single-particle properties and effective valley–valley exchange interactions in the valley-Heisenberg model $\mathcal{H}_v$ (4). (a) Local valley (Berry) flux $\Phi(\boldsymbol{r}, E)$ near half filling (at energy $E \simeq -0.1t_\perp$), averaged over the microscopic scale of model (1) including both layers, see Eq. (5). The staggered flux is largest in AB/BA regions and vanishes in the AA regions. (b) Flatband as obtained from the microscopic model (1) (top) compared with the phenomenological model (2) (bottom) at finite interlayer bias $V = 0.33t_\perp$, and with $\gamma_1 = \gamma_2 = 0.07t_\perp$ and $\phi_1 = -\phi_2 = 0.7$. Note the difference with the $V = 0$ result in Fig. 2(c). (c)–(e) Isotropic (J_n), anisotropic (Δ_n), and antisymmetric (D_n) valley exchange couplings, cf. Eq. (4), for first and second neighbors ($n = 1, 2$) as interlayer bias V increases. The interlayer bias can enhance the first-neighbor hopping to the point where $\gamma_1 = \gamma_2$ and $\phi_1 = -\phi_2$, resulting in exchange couplings of the same magnitude for first and second neighbors (here at $V \simeq 0.33t_\perp$). (d) The numerical mean-field (MF) result (open circles) superimposed on the analytical result (solid and dashed lines) [58].

finite and increase appreciably. Thus, we find that the interlayer bias (i) increases the easy-plane exchange anisotropy (increasing Δ_n), (ii) decreases the overall tendency for anti-valley-magnetic order and geometric frustration (decreasing J_n), and (iii) increases canting (through D_n). Interestingly, this means that the interlayer bias switches between the two mechanisms responsible for valley spirals discussed above. Note that there is also a competition of canting between first- and second-neighbor orbital pairs that influences the length scale of the valley spiral, where in numerical mean-field calculations, we predominantly observed 120° nearest-neighbor or second-neighbor spiral structures (not shown here).

In contrast to spin, valley is an orbital degree of freedom, and thus provides an extra challenge when it comes to interpretation and experimental verification [52,74–83]. We propose to make use of the VHE, where band electrons from different valleys flow in opposite directions, leading to transverse charge-neutral valley currents [74,75,84]. These currents can be detected as they induce voltages in other regions of the material through the inverse VHE,

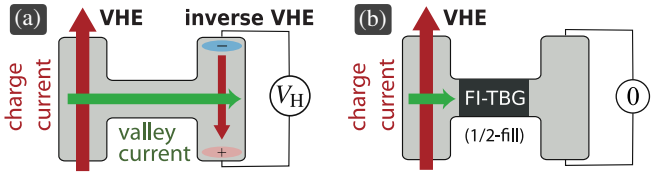

FIG. 4. Schematic setup for an experiment signaling the presence of a valley spiral state. (a) Standard four-terminal device, with valley Hall effect (VHE) driven by a charge current and inverse VHE driven by a valley current and producing a finite voltage V_H [74,75]. (b) FI-encapsulated TBG (FI-TBG) at half filling of the flatband acts as a filter blocking the valley current and suppresses the voltage V_H of the inverse VHE.

see Fig. 4(a). Such a four-terminal setup can detect valley-correlated states through their impact on valley Hall measurements, e.g., when embedding our system into a suitable device geometry, see Fig. 4(b). For example, a valley magnet ($\langle v_I^z \rangle \neq 0$) acts as a valley filter and can be used to suppress the valley Hall signal for one valley but not the other. In our case, we expect the planar valley spiral ($\langle v_I^z \rangle = 0$) to act as a "coherent valley mixer" [85–87]. This would strongly suppress the valley Hall signal when the chemical potential is swept to approach half filling of the flatband, thus providing an experimental signature for spontaneous valley mixing. Distinguishing noncollinear from collinear valley-coherent states is more involved, but could be achieved by studying valley decoherence, which is enhanced for noncollinear states.

To conclude, we put forward a minimal graphene-based heterostructure displaying spontaneous valley mixing, opening up a pathway to explore valley-correlated states in twisted graphene multilayers. Going beyond this work, we observe that our FI-encapsulated TBG and twisted *double*-bilayer graphene (TDBG) have analogous electronic band structures, except that spin in the former replaces the additional graphene layers in the latter. This remarkable similarity suggests that our system is a candidate for valley-analogous realizations of recent proposals and observations [88–90] for TDBG, including correlated insulators [7,91], magnetic superconductors [89], fractional quantum Hall states [92–95], and valley liquids [13,96–98].

We acknowledge funding from the Swiss National Science Foundation (SNSF) through division II, the careers committee, and through NCCR QSIT. J. L. L. acknowledges the computational resources provided by the Aalto Science-IT project and funding from the Academy of Finland.

*Corresponding author.
wolft@phys.ethz.ch

[1] Y. Cao, V. Fatemi, S. Fang, K. Watanabe, T. Taniguchi, E. Kaxiras, and P. Jarillo-Herrero, Unconventional superconductivity in magic-angle graphene superlattices, Nature (London) **556**, 43 (2018).
[2] M. Yankowitz, S. Chen, H. Polshyn, Y. Zhang, K. Watanabe, T. Taniguchi, D. Graf, A. F. Young, and C. R. Dean, Tuning superconductivity in twisted bilayer graphene, Science **363**, 1059 (2019).
[3] X. Lu, P. Stepanov, W. Yang, M. Xie, M. A. Aamir, I. Das, C. Urgell, K. Watanabe, T. Taniguchi, G. Zhang, A. Bachtold, A. H. MacDonald, and D. K. Efetov, Superconductors, orbital magnets and correlated states in magic-angle bilayer graphene, Nature (London) **574**, 653 (2019).
[4] H. S. Arora, R. Polski, Y. Zhang, A. Thomson, Y. Choi, H. Kim, Z. Lin, I. Z. Wilson, X. Xu, J.-H. Chu, K. Watanabe, T. Taniguchi, J. Alicea, and S. Nadj-Perge, Superconductivity in metallic twisted bilayer graphene stabilized by WSe_2, Nature (London) **583**, 379 (2020).
[5] Y. Cao, D. Chowdhury, D. Rodan-Legrain, O. Rubies-Bigorda, K. Watanabe, T. Taniguchi, T. Senthil, and P. Jarillo-Herrero, Strange Metal in Magic-Angle Graphene with near Planckian Dissipation, Phys. Rev. Lett. **124**, 076801 (2020).
[6] Y. Cao, V. Fatemi, A. Demir, S. Fang, S. L. Tomarken, J. Y. Luo, J. D. Sanchez-Yamagishi, K. Watanabe, T. Taniguchi, E. Kaxiras, R. C. Ashoori, and P. Jarillo-Herrero, Correlated insulator behaviour at half-filling in magic-angle graphene superlattices, Nature (London) **556**, 80 (2018).
[7] Y. Cao, D. Rodan-Legrain, O. Rubies-Bigorda, J. M. Park, K. Watanabe, T. Taniguchi, and P. Jarillo-Herrero, Tunable correlated states and spin-polarized phases in twisted bilayer–bilayer graphene, Nature (London) **583**, 215 (2020).
[8] M. Serlin, C. L. Tschirhart, H. Polshyn, Y. Zhang, J. Zhu, K. Watanabe, T. Taniguchi, L. Balents, and A. F. Young, Intrinsic quantized anomalous Hall effect in a moiré heterostructure, Science **367**, 900 (2019).
[9] J. D. Sanchez-Yamagishi, J. Y. Luo, A. F. Young, B. M. Hunt, K. Watanabe, T. Taniguchi, R. C. Ashoori, and P. Jarillo-Herrero, Helical edge states and fractional quantum Hall effect in a graphene electron–hole bilayer, Nat. Nanotechnol. **12**, 118 (2016).
[10] M.-S. Choi, R. López, and R. Aguado, Su(4) Kondo Effect in Carbon Nanotubes, Phys. Rev. Lett. **95**, 067204 (2005).
[11] P. Jarillo-Herrero, J. Kong, H. S. Van Der Zant, C. Dekker, L. P. Kouwenhoven, and S. De Franceschi, Orbital Kondo effect in carbon nanotubes, Nature (London) **434**, 484 (2005).
[12] C. Xu and L. Balents, Topological Superconductivity in Twisted Multilayer Graphene, Phys. Rev. Lett. **121**, 087001 (2018).
[13] W. M. H. Natori, R. Nutakki, R. G. Pereira, and E. C. Andrade, SU(4) Heisenberg model on the honeycomb lattice with exchange-frustrated perturbations: Implications for twistronics and Mott insulators, Phys. Rev. B **100**, 205131 (2019).
[14] N. Bultinck, E. Khalaf, S. Liu, S. Chatterjee, A. Vishwanath, and M. P. Zaletel, Ground State and Hidden Symmetry of Magic-Angle Graphene at Even Integer Filling, Phys. Rev. X **10**, 031034 (2020).
[15] H. Ochoa, Strain-induced excitonic instability in twisted bilayer graphene, Phys. Rev. B **102**, 201107 (2020).
[16] E. Khalaf, S. Chatterjee, N. Bultinck, M. P. Zaletel, and A. Vishwanath, Charged skyrmions and topological origin

of superconductivity in magic angle graphene, arXiv: 2004.00638.
[17] M. Christos, S. Sachdev, and M. S. Scheurer, Superconductivity, correlated insulators, and Wess-Zumino-Witten terms in twisted bilayer graphene, Proc. Natl. Acad. Sci. U.S.A. **117**, 29543 (2020).
[18] C. L. Kane and E. J. Mele, Quantum Spin Hall Effect in Graphene, Phys. Rev. Lett. **95**, 226801 (2005).
[19] Z. Qiao, S. A. Yang, W. Feng, W.-K. Tse, J. Ding, Y. Yao, J. Wang, and Q. Niu, Quantum anomalous Hall effect in graphene from Rashba and exchange effects, Phys. Rev. B **82**, 161414(R) (2010).
[20] Z. Wang, C. Tang, R. Sachs, Y. Barlas, and J. Shi, Proximity-Induced Ferromagnetism in Graphene Revealed by the Anomalous Hall Effect, Phys. Rev. Lett. **114**, 016603 (2015).
[21] Y. Yao, F. Ye, X.-L. Qi, S.-C. Zhang, and Z. Fang, Spin-orbit gap of graphene: First-principles calculations, Phys. Rev. B **75**, 041401(R) (2007).
[22] A. Avsar, H. Ochoa, F. Guinea, B. Özyilmaz, B. J. van Wees, and I. J. Vera-Marun, Colloquium: Spintronics in graphene and other two-dimensional materials, Rev. Mod. Phys. **92**, 021003 (2020).
[23] M. H. D. Guimarães, P. J. Zomer, J. Ingla-Aynés, J. C. Brant, N. Tombros, and B. J. van Wees, Controlling Spin Relaxation in Hexagonal BN-Encapsulated Graphene with a Transverse Electric Field, Phys. Rev. Lett. **113**, 086602 (2014).
[24] Z. Wang, D.-K. Ki, J. Y. Khoo, D. Mauro, H. Berger, L. S. Levitov, and A. F. Morpurgo, Origin and Magnitude of "Designer" Spin-Orbit Interaction in Graphene on Semiconducting Transition Metal Dichalcogenides, Phys. Rev. X **6**, 041020 (2016).
[25] J. Island, X. Cui, C. Lewandowski, J. Y. Khoo, E. Spanton, H. Zhou, D. Rhodes, J. Hone, T. Taniguchi, K. Watanabe, L. Levitov, M. Zaletel, and A. Young, Spin-orbit-driven band inversion in bilayer graphene by the van der Waals proximity effect, Nature (London) **571**, 85 (2019).
[26] D. Wang, S. Che, G. Cao, R. Lyu, K. Watanabe, T. Taniguchi, C. N. Lau, and M. Bockrath, Quantum Hall effect measurement of spin-orbit coupling strengths in ultraclean bilayer graphene/WSe_2 heterostructures, Nano Lett. **19**, 7028 (2019).
[27] T. Wang, N. Bultinck, and M. P. Zaletel, Flat band topology of magic angle graphene on a transition metal dichalcogenide, Phys. Rev. B **102**, 235146 (2020).
[28] J. Zhang, B. Zhao, T. Zhou, Y. Xue, C. Ma, and Z. Yang, Strong magnetization and Chern insulators in compressed graphene/CrI_3 van der Waals heterostructures, Phys. Rev. B **97**, 085401 (2018).
[29] Y. Choi, J. Kemmer, Y. Peng, A. Thomson, H. Arora, R. Polski, Y. Zhang, H. Ren, J. Alicea, G. Refael, F. Oppen, K. Watanabe, T. Taniguchi, and S. Nadj-Perge, Electronic correlations in twisted bilayer graphene near the magic angle, Nat. Phys. **15**, 1174 (2019).
[30] D. Zhong, K. L. Seyler, X. Linpeng, R. Cheng, N. Sivadas, B. Huang, E. Schmidgall, T. Taniguchi, K. Watanabe, M. A. McGuire, W. Yao, D. Xiao, K.-M. C. Fu, and X. Xu, Van der Waals engineering of ferromagnetic semiconductor heterostructures for spin and valleytronics, Sci. Adv. **3**, e1603113 (2017).
[31] H. X. Yang, A. Hallal, D. Terrade, X. Waintal, S. Roche, and M. Chshiev, Proximity Effects Induced in Graphene by Magnetic Insulators: First-Principles Calculations on Spin Filtering and Exchange-Splitting Gaps, Phys. Rev. Lett. **110**, 046603 (2013).
[32] S. Singh, J. Katoch, T. Zhu, K.-Y. Meng, T. Liu, J. T. Brangham, F. Yang, M. E. Flatté, and R. K. Kawakami, Strong Modulation of Spin Currents in Bilayer Graphene by Static and Fluctuating Proximity Exchange Fields, Phys. Rev. Lett. **118**, 187201 (2017).
[33] K. Zollner, P. E. Faria Junior, and J. Fabian, Proximity exchange effects in $MoSe_2$ and WSe_2 heterostructures with CrI_3: Twist angle, layer, and gate dependence, Phys. Rev. B **100**, 085128 (2019).
[34] M. Peralta, E. Medina, and F. Mireles, Proximity-induced exchange and spin-orbit effects in graphene on Ni and Co, Phys. Rev. B **99**, 195452 (2019).
[35] W. Han, R. K. Kawakami, M. Gmitra, and J. Fabian, Graphene spintronics, Nat. Nanotechnol. **9**, 794 (2014).
[36] C. K. Safeer, J. Ingla-Aynés, F. Herling, J. H. Garcia, M. Vila, N. Ontoso, M. R. Calvo, S. Roche, L. E. Hueso, and F. Casanova, Room-temperature spin Hall effect in graphene/MoS_2 van der Waals heterostructures, Nano Lett. **19**, 1074 (2019).
[37] B. Yang, M. Lohmann, D. Barroso, I. Liao, Z. Lin, Y. Liu, L. Bartels, K. Watanabe, T. Taniguchi, and J. Shi, Strong electron-hole symmetric Rashba spin-orbit coupling in graphene/monolayer transition metal dichalcogenide heterostructures, Phys. Rev. B **96**, 041409(R) (2017).
[38] Y. S. Dedkov, M. Fonin, U. Rüdiger, and C. Laubschat, Rashba Effect in the Graphene/Ni(111) System, Phys. Rev. Lett. **100**, 107602 (2008).
[39] A. H. Castro Neto, F. Guinea, N. M. R. Peres, K. S. Novoselov, and A. K. Geim, The electronic properties of graphene, Rev. Mod. Phys. **81**, 109 (2009).
[40] S. Reich, J. Maultzsch, C. Thomsen, and P. Ordejón, Tight-binding description of graphene, Phys. Rev. B **66**, 035412 (2002).
[41] G. Trambly de Laissardière, D. Mayou, and L. Magaud, Localization of Dirac electrons in rotated graphene bilayers, Nano Lett. **10**, 804 (2010).
[42] P. Moon and M. Koshino, Optical absorption in twisted bilayer graphene, Phys. Rev. B **87**, 205404 (2013).
[43] E. Colomés and M. Franz, Antichiral Edge States in a Modified Haldane Nanoribbon, Phys. Rev. Lett. **120**, 086603 (2018).
[44] A. Ramires and J. L. Lado, Electrically Tunable Gauge Fields in Tiny-Angle Twisted Bilayer Graphene, Phys. Rev. Lett. **121**, 146801 (2018).
[45] A. Ramires and J. L. Lado, Impurity-induced triple point fermions in twisted bilayer graphene, Phys. Rev. B **99**, 245118 (2019).
[46] T. M. R. Wolf, J. L. Lado, G. Blatter, and O. Zilberberg, Electrically Tunable Flat Bands and Magnetism in Twisted Bilayer Graphene, Phys. Rev. Lett. **123**, 096802 (2019).
[47] A. O. Sboychakov, A. L. Rakhmanov, A. V. Rozhkov, and F. Nori, Electronic spectrum of twisted bilayer graphene, Phys. Rev. B **92**, 075402 (2015).

[48] J. M. B. Lopes dos Santos, N. M. R. Peres, and A. H. Castro Neto, Continuum model of the twisted graphene bilayer, Phys. Rev. B **86**, 155449 (2012).
[49] E. Suárez Morell, J. D. Correa, P. Vargas, M. Pacheco, and Z. Barticevic, Flat bands in slightly twisted bilayer graphene: Tight-binding calculations, Phys. Rev. B **82**, 121407(R) (2010).
[50] J. M. B. Lopes dos Santos, N. M. R. Peres, and A. H. Castro Neto, Graphene Bilayer with a Twist: Electronic Structure, Phys. Rev. Lett. **99**, 256802 (2007).
[51] R. Bistritzer and A. H. MacDonald, Moire bands in twisted double-layer graphene, Proc. Natl. Acad. Sci. U.S.A. **108**, 12233 (2011).
[52] P. San-Jose and E. Prada, Helical networks in twisted bilayer graphene under interlayer bias, Phys. Rev. B **88**, 121408(R) (2013).
[53] M. Koshino, N. F. Q. Yuan, T. Koretsune, M. Ochi, K. Kuroki, and L. Fu, Maximally Localized Wannier Orbitals and the Extended Hubbard Model for Twisted Bilayer Graphene, Phys. Rev. X **8**, 031087 (2018).
[54] J. Kang and O. Vafek, Symmetry, Maximally Localized Wannier States, and a Low-Energy Model for Twisted Bilayer Graphene Narrow Bands, Phys. Rev. X **8**, 031088 (2018).
[55] H. C. Po, L. Zou, A. Vishwanath, and T. Senthil, Origin of Mott Insulating Behavior and Superconductivity in Twisted Bilayer Graphene, Phys. Rev. X **8**, 031089 (2018).
[56] K. Hejazi, C. Liu, H. Shapourian, X. Chen, and L. Balents, Multiple topological transitions in twisted bilayer graphene near the first magic angle, Phys. Rev. B **99**, 035111 (2019).
[57] C. Gong and X. Zhang, Two-dimensional magnetic crystals and emergent heterostructure devices, Science **363**, eaav4450 (2019).
[58] See Supplemental Material at http://link.aps.org/supplemental/10.1103/PhysRevLett.126.056803 for more details on the effective model, mean-field approximation, and anisotropic valley-Heisenberg model.
[59] C. Cardoso, D. Soriano, N. A. García-Martínez, and J. Fernández-Rossier, Van der Waals Spin Valves, Phys. Rev. Lett. **121**, 067701 (2018).
[60] F. Guinea and N. R. Walet, Electrostatic effects, band distortions, and superconductivity in twisted graphene bilayers, Proc. Natl. Acad. Sci. U.S.A. **115**, 13174 (2018).
[61] P. Stepanov, I. Das, X. Lu, A. Fahimniya, K. Watanabe, T. Taniguchi, F. H. L. Koppens, J. Lischner, L. Levitov, and D. K. Efetov, Untying the insulating and superconducting orders in magic-angle graphene, Nature (London) **583**, 375 (2020).
[62] Z. A. H. Goodwin, F. Corsetti, A. A. Mostofi, and J. Lischner, Twist-angle sensitivity of electron correlations in moiré graphene bilayers, Phys. Rev. B **100**, 121106(R) (2019).
[63] J. M. Pizarro, M. Rösner, R. Thomale, R. Valentí, and T. O. Wehling, Internal screening and dielectric engineering in magic-angle twisted bilayer graphene, Phys. Rev. B **100**, 161102(R) (2019).
[64] J. Hubbard, Electron correlations in narrow energy bands, Proc. R. Soc. A **276**, 238 (1963).
[65] P. Sahebsara and D. Sénéchal, Hubbard Model on the Triangular Lattice: Spiral Order and Spin Liquid, Phys. Rev. Lett. **100**, 136402 (2008).
[66] A. Vaezi, M. Mashkoori, and M. Hosseini, Phase diagram of the strongly correlated Kane-Mele-Hubbard model, Phys. Rev. B **85**, 195126 (2012).
[67] K. Li, S.-L. Yu, Z.-L. Gu, and J.-X. Li, Phase diagram and topological phases in the triangular lattice Kitaev-Hubbard model, Phys. Rev. B **94**, 125120 (2016).
[68] K. Misumi, T. Kaneko, and Y. Ohta, Mott transition and magnetism of the triangular-lattice Hubbard model with next-nearest-neighbor hopping, Phys. Rev. B **95**, 075124 (2017).
[69] J. R. Schrieffer and P. A. Wolff, Relation between the Anderson and Kondo Hamiltonians, Phys. Rev. **149**, 491 (1966).
[70] We introduce the nomenclature (anti)valley magnetic for the valley sector in distinction to (anti)ferromagnetism in the spin sector.
[71] S. Heinze, K. Von Bergmann, M. Menzel, J. Brede, A. Kubetzka, R. Wiesendanger, G. Bihlmayer, and S. Blügel, Spontaneous atomic-scale magnetic skyrmion lattice in two dimensions, Nat. Phys. **7**, 713 (2011).
[72] K.-T. Chen and P. A. Lee, Unified formalism for calculating polarization, magnetization, and more in a periodic insulator, Phys. Rev. B **84**, 205137 (2011).
[73] A. L. R. Manesco, J. L. Lado, E. V. Ribeiro, G. Weber, and J. Rodrigues, Durval, Correlations in the elastic Landau level of a graphene/$NbSe_2$ van der Waals heterostructure, 2D Mater. **8**, 015011 (2021).
[74] D. Xiao, W. Yao, and Q. Niu, Valley-Contrasting Physics in Graphene: Magnetic Moment and Topological Transport, Phys. Rev. Lett. **99**, 236809 (2007).
[75] M. Yamamoto, Y. Shimazaki, I. V. Borzenets, and S. Tarucha, Valley Hall effect in two-dimensional hexagonal lattices, J. Phys. Soc. Jpn. **84**, 121006 (2015).
[76] Y. Jiang, T. Low, K. Chang, M. I. Katsnelson, and F. Guinea, Generation of Pure Bulk Valley Current in Graphene, Phys. Rev. Lett. **110**, 046601 (2013).
[77] T. L. Linnik, Photoinduced valley currents in strained graphene, Phys. Rev. B **90**, 075406 (2014).
[78] J. H. J. Martiny, K. Kaasbjerg, and A.-P. Jauho, Tunable valley Hall effect in gate-defined graphene superlattices, Phys. Rev. B **100**, 155414 (2019).
[79] V. H. Nguyen, S. Dechamps, P. Dollfus, and J.-C. Charlier, Valley Filtering and Electronic Optics Using Polycrystalline Graphene, Phys. Rev. Lett. **117**, 247702 (2016).
[80] A. R. Akhmerov and C. W. J. Beenakker, Detection of Valley Polarization in Graphene by a Superconducting Contact, Phys. Rev. Lett. **98**, 157003 (2007).
[81] P. Rickhaus, J. Wallbank, S. Slizovskiy, R. Pisoni, H. Overweg, Y. Lee, M. Eich, M.-H. Liu, K. Watanabe, T. Taniguchi, T. Ihn, and K. Ensslin, Transport through a network of topological channels in twisted bilayer graphene, Nano Lett. **18**, 6725 (2018).
[82] S. G. Xu, A. I. Berdyugin, P. Kumaravadivel, F. Guinea, R. K. Kumar, D. A. Bandurin, S. V. Morozov, W. Kuang, B. Tsim, S. Liu, J. H. Edgar, I. V. Grigorieva, V. I. Fal'ko, M. Kim, and A. K. Geim, Giant oscillations in a triangular network of one-dimensional states in marginally twisted graphene, Nat. Commun. **10**, 4008 (2019).
[83] S. Huang, K. Kim, D. K. Efimkin, T. Lovorn, T. Taniguchi, K. Watanabe, A. H. MacDonald, E. Tutuc, and B. J. LeRoy,

Topologically Protected Helical States in Minimally Twisted Bilayer Graphene, Phys. Rev. Lett. **121**, 037702 (2018).

[84] Y. Shimazaki, M. Yamamoto, I. V. Borzenets, K. Watanabe, T. Taniguchi, and S. Tarucha, Generation and detection of pure valley current by electrically induced Berry curvature in bilayer graphene, Nat. Phys. **11**, 1032 (2015).

[85] L. Meng, Z.-D. Chu, Y. Zhang, J.-Y. Yang, R.-F. Dou, J.-C. Nie, and L. He, Enhanced intervalley scattering of twisted bilayer graphene by periodic *AB* stacked atoms, Phys. Rev. B **85**, 235453 (2012).

[86] B. Yan, Q. Han, Z. Jia, J. Niu, T. Cai, D. Yu, and X. Wu, Electrical control of intervalley scattering in graphene via the charge state of defects, Phys. Rev. B **93**, 041407(R) (2016).

[87] A. F. Morpurgo and F. Guinea, Intervalley Scattering, Long-Range Disorder, and Effective Time-Reversal Symmetry Breaking in Graphene, Phys. Rev. Lett. **97**, 196804 (2006).

[88] C. Shen, Y. Chu, Q. Wu, N. Li, S. Wang, Y. Zhao, J. Tang, J. Liu, J. Tian, K. Watanabe, T. Taniguchi, R. Yang, Z. Y. Meng, D. Shi, O. V. Yazyev, and G. Zhang, Correlated states in twisted double bilayer graphene, Nat. Phys. **16**, 520 (2020).

[89] X. Liu, Z. Hao, E. Khalaf, J. Y. Lee, K. Watanabe, T. Taniguchi, A. Vishwanath, and P. Kim, Spin-polarized correlated insulator and superconductor in twisted double bilayer graphene, Nature (London) **583**, 221 (2020).

[90] M. He, Y. Li, J. Cai, Y. Liu, K. Watanabe, T. Taniguchi, X. Xu, and M. Yankowitz, Tunable correlation-driven symmetry breaking in twisted double bilayer graphene, Nat. Phys. **17**, 26 (2021).

[91] G. W. Burg, J. Zhu, T. Taniguchi, K. Watanabe, A. H. MacDonald, and E. Tutuc, Correlated Insulating States in Twisted Double Bilayer Graphene, Phys. Rev. Lett. **123**, 197702 (2019).

[92] A. Abouelkomsan, Z. Liu, and E. J. Bergholtz, Particle-Hole Duality, Emergent Fermi Liquids, and Fractional Chern Insulators in Moiré Flatbands, Phys. Rev. Lett. **124**, 106803 (2020).

[93] Z. Liu, A. Abouelkomsan, and E. J. Bergholtz, Gate-Tunable Fractional Chern Insulators in Twisted Double Bilayer Graphene, Phys. Rev. Lett. **126**, 026081 (2021).

[94] P. J. Ledwith, G. Tarnopolsky, E. Khalaf, and A. Vishwanath, Fractional Chern insulator states in twisted bilayer graphene: An analytical approach, Phys. Rev. Research **2**, 023237 (2020).

[95] C. Repellin and T. Senthil, Chern bands of twisted bilayer graphene: Fractional Chern insulators and spin phase transition, Phys. Rev. Research **2**, 023238 (2020).

[96] X.-C. Wu, A. Keselman, C.-M. Jian, K. A. Pawlak, and C. Xu, Ferromagnetism and spin-valley liquid states in moiré correlated insulators, Phys. Rev. B **100**, 024421 (2019).

[97] V. Y. Irkhin and Y. N. Skryabin, Dirac points, spinons, and spin liquid in twisted bilayer graphene, JETP Lett. **107**, 651 (2018).

[98] L. A. Gonzalez-Arraga, J. L. Lado, F. Guinea, and P. San-Jose, Electrically Controllable Magnetism in Twisted Bilayer Graphene, Phys. Rev. Lett. **119**, 107201 (2017).